Surface-Mounted Ka-Band Vivaldi Antenna Array

HENRI KÄHKÖNEN [1,2], **JUHA ALA-LAURINAHO** [1], **AND VILLE VIIKARI** [1] (Senior Member, IEEE)

[1]Department of Electronics and Nanoengineering, Aalto University, 00076 Espoo, Finland

[2]Saab Finland Oy, 00100 Helsinki, Finland

CORRESPONDING AUTHOR: H. KÄHKÖNEN (e-mail: henri.kahkonen@aalto.fi)

ABSTRACT The first electrically steerable dual-polarized Ka-band Vivaldi antenna array with connector-less, surface-mount interface is developed. The antenna interface includes integrated coaxial feed lines within the antenna element structure and contact pads on the PCB. The antenna array covers the frequency range from 26 to 40 GHz with a beam steering range of approximately ±60° in the elementary planes and ±50° in the diagonal plane, having less than 3 dB of scan loss. The 8×8 antenna array is manufactured with a feeding network for one polarization, and the operation of the interface and the electrical beam steering is demonstrated. Measurements are used to characterize the manufactured feed network, the gain of the antenna array and the steering range. The measured gain is between 19 and 22 dB, agreeing very well with the simulation and implying that the antenna interface operates properly. Furthermore, the antenna scan measurements agree with the simulation results.

INDEX TERMS 5G, antenna array, electronically scanned array, flared-notch antenna, Ka band, phased array, tapered slot, Vivaldi antenna, wideband, surface-mounted antenna array.

I. INTRODUCTION

VIVALDI antenna elements have been studied and used in electrically steerable wideband arrays from low microwave frequencies generally up to the K-band, but designs with limited number of elements, i.e., linear arrays, have been published for higher frequencies [1]–[12]. Vivaldi antennas have many advantages, such as a wide operation band, small inter-element spacing and large beam steering range, and could therefore be used in many emerging applications, such as mm-wave wireless communications.

A challenge in using Vivaldi elements in antenna arrays outside linear arrays at mm-wave frequencies is the interface between the antenna elements and the electronics where connectors have been previously used. When the operation frequency increases, the available volume to implement dedicated RF connectors decreases. For example, the inter-element distance should be less than 3.8 mm at 40 GHz for grating-lobe-free operation. In the case of a dual-polarized array, two connectors cannot occupy an area of more than 3.8×3.8 mm area of the antenna. However, even the smallest WSMP and SMPS connectors require 2.5mm×2.5mm each, making fitting them in the available space nearly impossible. The challenge becomes even more demanding at higher frequencies. Additionally, connectors are expensive and require much space also on the PCB, significantly increasing the bulkiness.

However, these kinds of separate fully metallic antenna arrays add another step of manufacturing when they are compared to planar antennas integrated on PCBs which have already been studied at Ka band [13]–[18]. While the planar antennas are in most cases easily included in the regular PCB manufacturing process, they can also include multiple metal and substrate layers increasing the complexity of the manufacturing. Typically, planar antennas cannot provide comparable bandwidth, efficiency, or beam-steering range. The planar array designs often have a bandwidth of less than 15% or they have a limited beam-steering range. Table 1 shows a comparison of the antenna array presented in this work and some state-of-the-art, dual-polarized, planar phased array designs at Ka-band. While the beamsteering range of the other planar antenna design in the comparison is also advertised as ±60°, the polarization purity of the antenna begins to decrease already after 30°. In the second array design, the element spacing is such that ±38° beam

TABLE 1. Performance comparison with recent prior articles at Ka band.

	This work	[13]	[14]
Frequency (GHz)	26–40	29.5–30	26–30
Beam-steering range (°):			
$\phi=0°$ plane	±60	±60	±45
$\phi=90°$ plane	±60	±60	±45
element spacing (λ)	0.51	0.5	0.66
Efficiency (%)	>90	not mentioned	66–82
Polarization	Dual LP	Dual CP	Dual LP

steering gives rise to a grating lobe inside the visible range at 28 GHz. Additionally, microstrip patch antennas can often have strong electric fields inside lossy substrates decreasing the efficiency.

A promising Vivaldi-array design for 26–40 GHz frequency with a connector-less interface to the PCB was presented in [19]. In this design, the metallic antenna array is connected to the PCB with through-hole technology. The array involves feed pins that are inserted into holes in the PCB and soldered to pads on the bottom side of the PCB. Through holes, however, introduce many challenges. First, since the pins go through the PCB fitting the feeding network to the array is challenging. Second, aluminium is preferred as the antenna material due to its good electrical conductivity and mechanical properties facilitating manufacturing, but soldering aluminum pins to copper pads requires a special process. Additionally, no electrical beam-steering was demonstrated.

In this article, we extend the design further and demonstrate electrical beam-steering using element-specific phase shifters. The antenna-PCB interface is redesigned to allow solder-less surface mounting of the antenna on the PCB. The novel connection is realized through capacitive coupling between the coaxial feeds of the antenna and the feeding pads on the PCB, as shown in Fig. 1. Furthermore, the PCB pads and antenna transition is designed to allow reasonable manufacturing and antenna alignment tolerance without performance degradation. When the metallic antenna is mounted directly on top of the PCB, the antenna structure could additionally be used to dissipate some of the heat produced by the electronic components on the PCB.

This article is organized as follows: the antenna array structure, the antenna-PCB interface, and the manufactured feed network are presented in Section II; the simulations of the interface and the antenna array are presented with measured results of the antenna performance in Section III; and Section IV concludes this article.

II. THE ANTENNA ARRAY STRUCTURE, INTERFACE, AND FEEDING NETWORK

The Vivaldi-antenna elements are manufactured either on substrates by conventional PCB manufacturing techniques, or they are machined out of metal. In both cases, each of the array elements is often connected through a separate RF-connector and possibly a cable to a PCB containing the RF-components and electronics such as amplifiers, phase shifters, and AD/DA-converters.
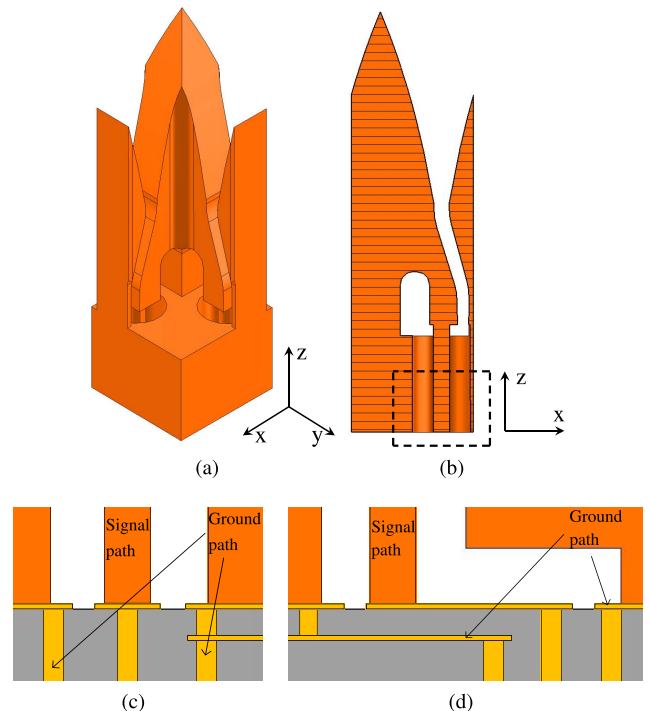
FIGURE 1. (a) An illustration of the antenna-element model, (b) planar cut of the antenna-element model with a box highlighting the coaxial antenna feed, and simplified illustrations of the two different interfaces between the antenna coaxial feed (inside the box) and the PCB: (c) the direct interface and (d) the indirect interface. In the interface illustrations, the antenna metal is colored orange, copper on the PCB yellow, and the PCB substrate gray.

The antenna-array geometry used here is somewhat similar to the fully metallic structure that was previously used at lower frequencies with a separate RF-connector behind each antenna element [4]–[6]. Some other Vivaldi-antenna designs also use separate RF connectors to feed each antenna element [7], [8], but beyond 30 GHz the size of the RF connectors may become a problem. The antenna-element geometry used here and the single element measurements in the Ka band have been previously presented in [19], where the operation of the antenna element was confirmed by comparing unit-cell and single-element simulations with measurements of selected elements in different locations in the antenna aperture.

One distinct difference between the antenna-element design here and previous studies at lower frequencies is the lack of suitable RF connectors that could be fit under the antenna-array element due to the small element size 3.8 mm × 3.8 mm. Thus, an integrated solution is used, where the coaxial antenna feed is included in the antenna structure itself. In such a structure, the antenna feed is a simple coaxial pin and an outer conductor integrated into the antenna ground plane that can be placed on top of corresponding pads on a PCB. The whole antenna, including the feed pin, can be manufactured from a single piece of metal with a combination of wire electric discharge machining (WEDM) and conventional machining. However, the same structure could also be manufactured with additive manufacturing after small

modifications to greatly decrease the manufacturing cost, time, and expertise required by WEDM.

The primary novel aspect of our antenna design is that the whole connectorless Vivaldi array can be surface mounted on a PCB with proper feed pads. The connection can be capacitive so that there is no need to solder or glue the element. However, soldering or gluing the array to the PCB will increase the realiability of the connection.

A. ANTENNA-ELEMENT INTERFACE

Due to the small inter-element spacing at 40 GHz, an interface without connectors is required. One of the key points of the interface design here is to keep the structure as simple as possible so as to avoid the use of additional parts. This eliminates the need to manufacture the small and precise parts required for mm-wave frequencies, and simplifies the final assembly of the antenna and the electronics.

The antenna-PCB integration method is adapted from the application of direct surface-mounted PCB connectors, where the center conductor is attached against a pad on the PCB and the outer conductor is attached to a pad around the center pad. Instead of using a separate connector, the interface can be directly integrated in the antenna array structure.

The interface can be implemented, for example, with the two different ways illustrated in Fig. 1 (c) and (d).

In the direct interface type, the signal path continues directly from the interface pad on the top layer of the PCB to another layer, either to a stripline in an inside layer or to a microstrip line on the other side of the PCB. A via between the interface pad and an inner layer is used to achieve this. Additionally, grounding vias around the signal via ensure that the signal ground is effectively transferred between the layers.

In the indirect transition model, the signal is first transferred to a microstrip on the top side of the PCB and then to another layer through vias. The indirect transition can result in a simpler PCB design since distributing the transition through the PCB to the desired places without striplines inside them is easier. On the other hand, cavities are necessary in the antenna structure corresponding to the microstrip lines, as shown in Fig. 1(d).

B. FEED-NETWORK PCB

The small inter-element spacing prevents the use of connectors and cables to measure each of the elements separately. To test the operation of the antenna array, a feeding network for single polarization is designed and manufactured. Since the antenna is polarization-symmetric, we characterize its operation only at a single polarization.

The coaxial feeds of the unused polarization are terminated with matched loads fabricated of magnetically loaded RF absorber material (Eccosorb MF-117 [20]). The material is formed to a shape and inserted inside the coaxial feeds. The shape of the inserted absorber is optimized through simulations. Fig. 2 shows the found optimal shape taking into account the available space. The reflection is reduced
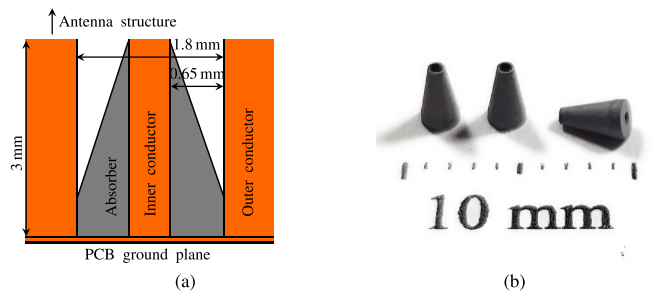

FIGURE 2. (a) An illustration of the coaxial antenna feed (box in Fig. 1(b)) with the absorber and (b) an image of the manufactured absorbers with a 10 mm scale for reference.

by more than 13 dB when comparing to the same coaxial line without the absorber.

Two different PCB designs are manufactured: one for measuring the broadside pattern of the antenna array to study the behavior of the feeding network and the other with inline phase shifters with each of the elements to demonstrate beam steering. Additionally, the feed network is designed such that the signal path to each element are close to equal in length. Both of these designs are otherwise identical, but in the fixed broadside pattern design the phase shifters are replaced with a straight microstrip lines, and the control lines for the phase shifters are removed. 5-Bit Qorvo TGP2102 phase shifters are used in the feed network with beam steering capability [21]. The used phase shifters support only 32-37 GHz band limiting the frequency range of the beam steering measurements.

The feeding network consists of a 1-to-64 power divider (composed of a tree of 1-to-2 Wilkinson dividers in five layers), a transition from the microstrip lines to a feeding pad on the opposite side of the PCB, and in the case of the beam-steerable model the phase shifters. The transition from the microstrip to the feeding pad first has a transition from the microstrip line through a via to a stripline inside the PCB followed by a final transition from the stripline through a via to the feeding pad. The entire feed network is shown in Fig. 3(a) and a more detailed illustration of the transitions in Fig. 3(b). In both figures the ground planes and the shielding vias are hidden to show the signal paths. All the signal paths inside the PCB are shielded with a ground plane and with a row of vias between two striplines to minimize coupling. Simulations indicate that the coupling between any two feed lines between the power dividers and the antenna feeds is at worst approximately −30 dB, and generally well below −40 dB.

The different signal layers are connected using 150 μm microvias. Microvias set some restrictions to the substrate thickness because they are realized with a laser, and the diameter of the via is related to the thickness of the material. To conform the designed transition with the selected manufacturing process, the PCB stack-up was designed to have eight metal layers with 125 μm substrates to accommodate the striplines inside the PCB. The design could also

(a)

(b)
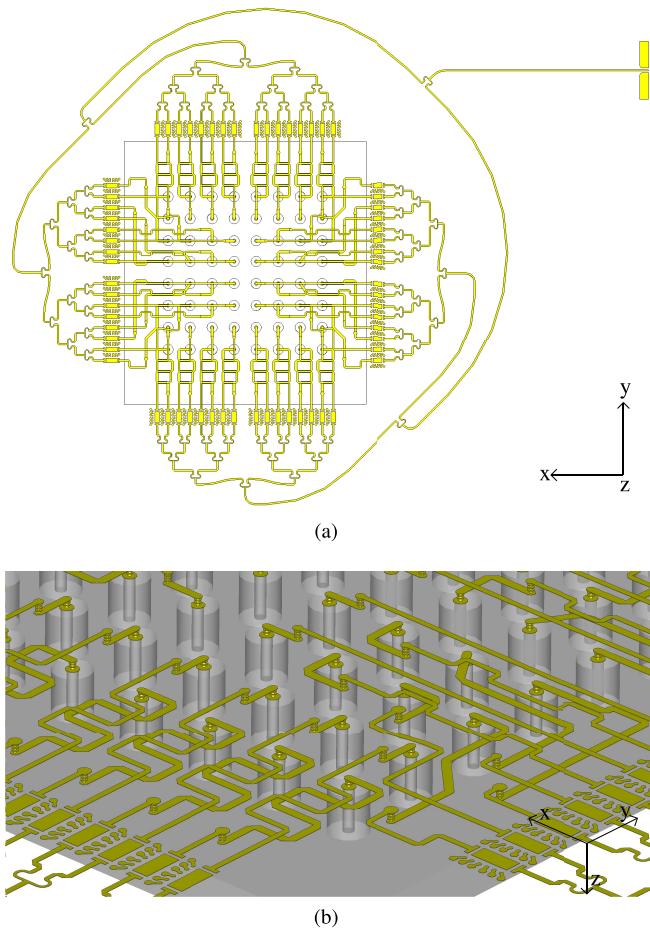
FIGURE 3. Illustration of the RF-lines in the designed feeding network for single polarization: (a) the whole feeding network and (b) one quarter of the transitions from the microstrip lines to the antenna feeding pads. Ground layers, ground vias, and substrates are not shown for clarity. Also, the coaxial feeds for the other polarization are omitted.
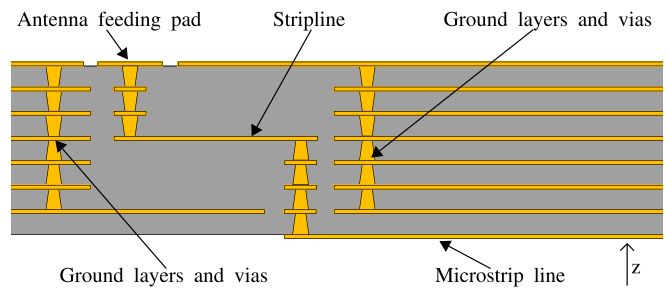
FIGURE 4. Illustration of the 8-layer PCB cross-section, where the general segments important to the RF performance of the feeding network are shown.

(a)

(b)
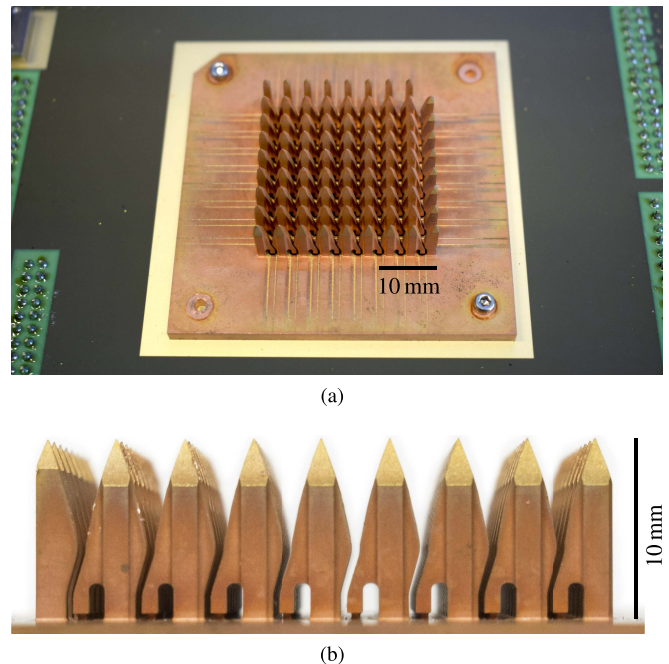
FIGURE 5. (a) Antenna array attached on the top of the test PCB and (b) the antenna element profile viewed from the side of the manufactured antenna array.

have been manufactured using six layers using a combination of drilled and laser vias. An illustration of the PCB cross-section is shown in Fig. 4, where the main RF design components in the transition are highlighted. The Panasonic Megtron7 substrate was selected due to its well-documented dielectric constant (3.3) and loss tangent (0.001-0.003) up to 50 GHz [22].

The feed network is simulated from the connector at the edge of the PCB to the antenna coaxial feed line including the transition from the PCB to the coaxial line. The simulation of the feed network is performed in CST Microwave Studio using a surface roughness of $0.6\,\mu m$ suggested by the PCB manufacturer. In the simulations, the insertion loss in the feed lines is 8.5 dB at 26 GHz and increases to 14.7 dB at 40 GHz from which approximately 74% is due to the conductor losses and 26% due to the dielectric losses. The feed line length including the microstrip lines and the striplines is 195 mm resulting in an average loss of 0.44 to 0.75 dB/cm. The standard deviation in the magnitude and the phase of the insertion loss between the antenna elements is approximately 0.5 dB and 10°, respectively.

C. MANUFACTURED ANTENNA ARRAY AND FEEDING NETWORK

The 8×8 dual-polarized antenna array was manufactured from copper using a combination of conventional machining and WEDM [19]. The whole array and a close-up image of the manufactured antenna-element profile is shown in Fig. 5. The inter-element spacing in the manufactured antenna array is 3.8 mm and the total height of the elements is 10 mm. The total area occupied by the antenna elements is $31.5\,mm\times31.5\,mm$ whereas the base plate is $60\,mm\times60\,mm$.

A part of the manufactured PCB and the phase shifters are shown in Fig. 6, where one of the four branches of the feeding network with the Wilkinson power dividers is visible.

The PCB manufacturer promises a nominal deviation in the line impedance at $50\,\Omega$ to be $\pm5\%$ for $300\,\mu m$ microstrip and stripline. The manufacturing tolerances of the antenna array are unknown, but under a microscope the dimensions appear to be very close to the designed dimensions.
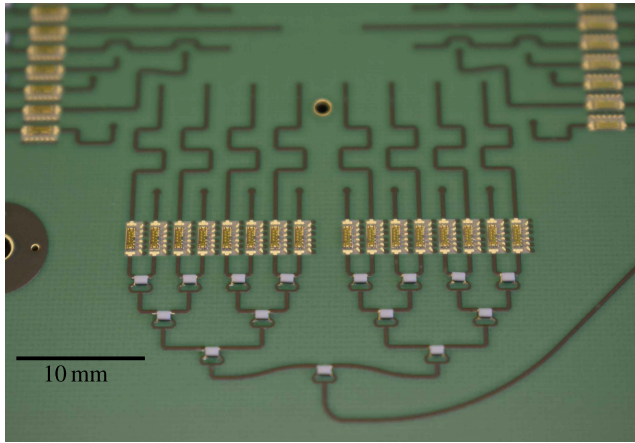
FIGURE 6. Part of the manufactured PCB where the phaseshifters and the resistors for the Wilkinson power dividers are attached. The phaseshifters have a spacing of 1.9 mm.

FIGURE 7. The near-field measurement setup. The antenna array under test (DUT) is on the left, and the probe scanning the antenna aperture is on the right. In addition to the probe, the measurement setup also includes a PNA, coaxial cables between the antennas and the PNA, the planar scanner moving the probe, and the computer controlling the scanner, PNA, and processing the results.
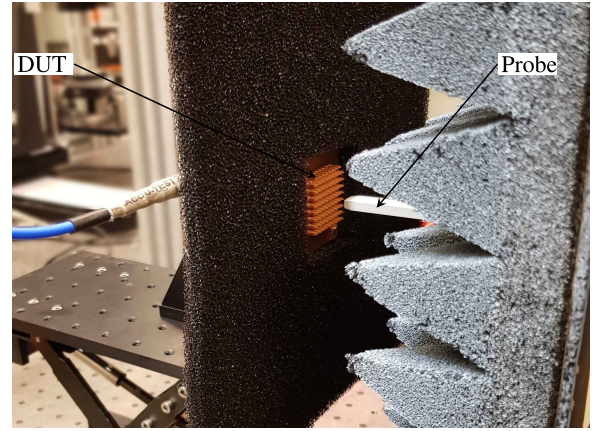
During all the measurements, the antenna is attached to the PCB only using screws, demonstrating the capacitive connection. In total, seven screws are used to secure the antenna and the PCB together. Two screws in the diagonal corners of the antenna base plate as shown in Fig. 5(a), and five smaller screws behind the antenna array going through the PCB to tapped holes in the antenna base plate.

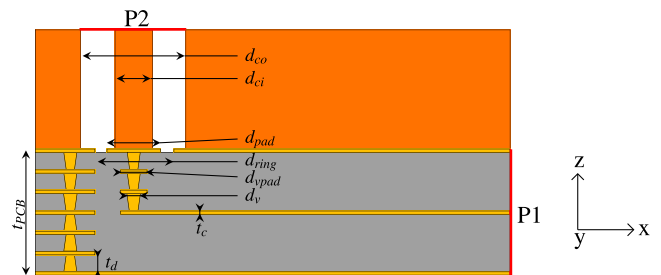## III. SIMULATION AND MEASUREMENT RESULTS

The structures presented here are first simulated and optimized separately. For example, the interface between the antenna element and the feeding network is initially simulated without the complete feed network. The 8×8 antenna array is simulated such that separate ports feed each of the coaxial lines feeding the antenna elements. This ensures that the results represent the antenna array itself, and we can neglect the effects of possible inaccuracies of the PCB, e.g., in the dielectric constant of the substrate and in the substrate or copper layer thicknesses.

The measurements are used to confirm the operation of the interface between the antenna and the PCB. Measurements are first performed using a planar near-field scanner with an open-ended waveguide (WR28) as a probe. Fig. 7 shows the near-field measurement setup where both the probe and the antenna are connected to a vector network analyzer (VNA). The probe movement and VNA are controlled by a computer. The electric field is measured in front of each antenna element and these results are used to solve the accurate phase responses of each antenna element. Then, the results are used to calibrate the phases in the beam-steerable test board for better evaluation of the performance.

The final measurements are performed both in an anechoic chamber in the far field and in the planar near-field scanner. The gain of the antenna array is measured in the anechoic chamber using a rectangular standard-gain horn (SGH) to calibrate the realized gain of the antenna-array structure. A simulated approximation of the losses in the feeding network is used to calculate the gain of the antenna where the feed

FIGURE 8. Illustration of the interface from the stripline to the coaxial antenna feed. The orange parts represent the base of the antenna array housing the coaxial pins feeding each antenna element. The gray area represents the PCB substrate, and the yellow areas represent the PCB conductors.

TABLE 2. Dimensions for PCB–antenna transition.

Parameter	Description	Value
d_{co}	Coaxial outer diameter	1.8 mm
d_{ci}	Coaxial inner diameter	0.5 mm
d_{pad}	Inner conductor pad diameter	0.6 mm
d_{ring}	Ground plane ring diameter	1.2 mm
d_{vpad}	Via pad diameter	250 μm
d_{v}	Via diameter	150 μm
t_{c}	Copper layer thickness	20 μm
t_{d}	Dielectric thickness	125 μm
t_{PCB}	Total PCB thickness	0.89 mm

network losses are omitted. The measurements, where the envelope of the co- and cross-polarized radiation patterns are solved, are performed in the planar near-field scanner to reduce the time required for the measurements.

A. ANTENNA INTERFACE SIMULATIONS

The transition from the PCB to the coaxial line in the antenna feed was analyzed with the structure shown in Fig. 8 with the dimensions shown in Table 2. In this structure, port P1 feeds a 50-Ω stripline, which is connected to a feeding pad that then connects to the center pin of the 75-Ω coaxial antenna feed. The coaxial line is finally terminated to another port, P2.
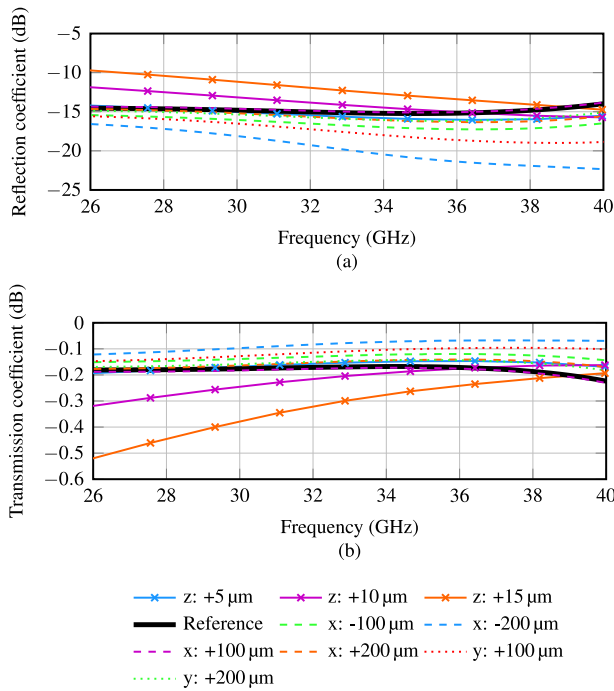
FIGURE 9. Simulation results of the sensitivity analysis when the feeding pin is moved with respect to the structures on the PCB. The reflection coefficient is shown in (a) and the transmission coefficient in (b).

In this test structure, the interface was designed to allow for reasonable manufacturing tolerances. For example, the gap between the feeding pad and the ground conductor on the top layer of the PCB is 0.3 mm. A smaller gap would result in a better performance but also to a higher sensitivity to a small misalignment between the two structures. The antenna elements were manufactured with an impedance of 75 Ω due to limitations in the manufacturing of the meandered slot line feeding the top of the antenna element.

The interface was first simulated in the case where the feeding pin and the PCB are lined up well and the pin is in the middle of the feeding pad. In the frequency range between 26 and 40 GHz, the reflection coefficient in the transition is, in this case, between −14 and −15 dB and the transmission coefficient for the transition is better than −0.2 dB, as is evident from Fig. 9. These values correspond well with theoretical transition where a step from 50 Ω to 75 Ω occurs.

In addition to the case where the pin is exactly on top of the feeding pad, a few cases where the pin is shifted with respect to the PCB were studied, since the coaxial feed can be slightly shifted along the surface of the PCB. Fig. 9 shows the simulated cases with a transversal shift along either y- or x-axis that indicate that a shift of 0.1 or 0.2 mm along either of these axes does not have a negative impact on the performance. In some cases, the performance of the transitions can even be seen to improve when the pin is shifted off center. This is caused by added reactance in the transition mitigating the mismatch between the 75-Ω coaxial

and 50-Ω stripline. In a case where the stripline and coaxial line are matched, the misalignment increases the reflection coefficient.

Since the transition can also be used without any solder between the PCB and the antenna, simulating the effect of a possible gap between the two structures on the performance is also important. These simulation results with a shift along the z-axis are also shown in Fig. 9. The results show that a gap of 5 μm or less does not negatively affect the performance, but an increase in the reflection coefficient can be seen when the gap is first increased to 10 μm and then to 15 μm.

B. FEED-NETWORK RESULTS WITHOUT PHASE SHIFTERS

The antenna array is simulated and measured with a broadside radiation pattern. In the simulations, each element is fed directly with a waveguide port behind the coaxial feed line, and the resulting element patterns are combined in post-processing. In the measurements, a feeding network where the phase shifters are replaced with microstrip lines is used. The comparison includes the broadside gain and the radiation patterns, whereas near-field measurements are used to assess the effect of the feed network.

First, the manufactured feeding network is characterized with near-field scanner measurements. The characterization is mainly used to calculate the realized phase shift caused by the feed network in each antenna element such that the performance of the feeding network can be assessed. The near-field scanner is used to measure the phase of the E-field in front of each antenna element (WR-28 open-ended waveguide at a distance of 2 mm). These results are compared to a simulation where zero phase is used to feed each antenna element. The E-field phase is similarly extracted from this initial simulation. The measured and simulated results are compared, and the differences are used as the phases in the feed of a new simulation. Finally, the result of the initial and the correlated simulation are compared with the measurement results.

The phase of the E-field across each of the antenna elements is shown in Fig. 10. The simulated results in the first column with identical signal in each antenna port results in a consistent phase across the antenna elements. The second column represent the measured results in which larger variation is present. In the first simulation, the phase across the antenna aperture varies less than 20° between any two elements, which is accounted for the slightly different coupling between the antenna elements at different locations in the array. However, variations of up to 80° are evident in the measured results. The difference between the simulation and measurement results can be explained by the variations in the manufactured feed-line lengths and the relative proportion of the stripline and microstrip line. The largest variation can be observed in the first and last rows of elements at the higher end of the frequency band. These elements all have identical feed lines which appears to be slightly longer
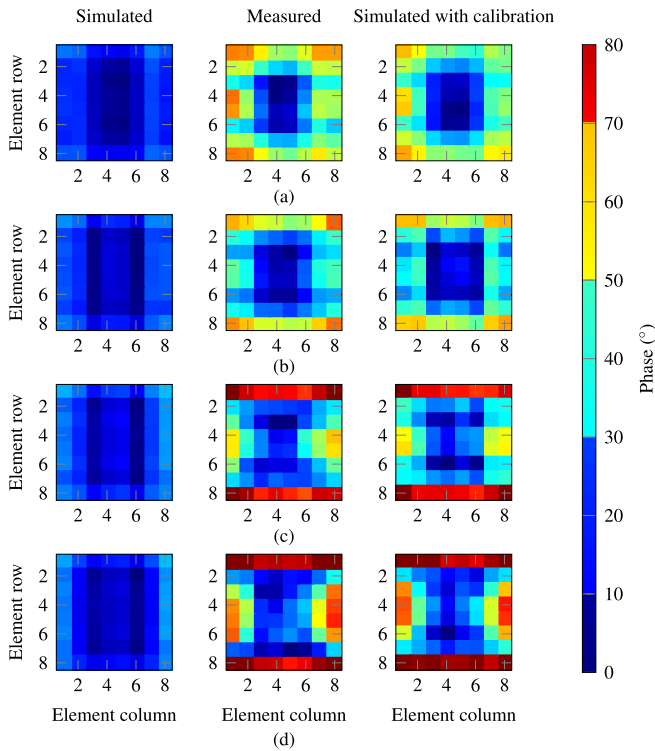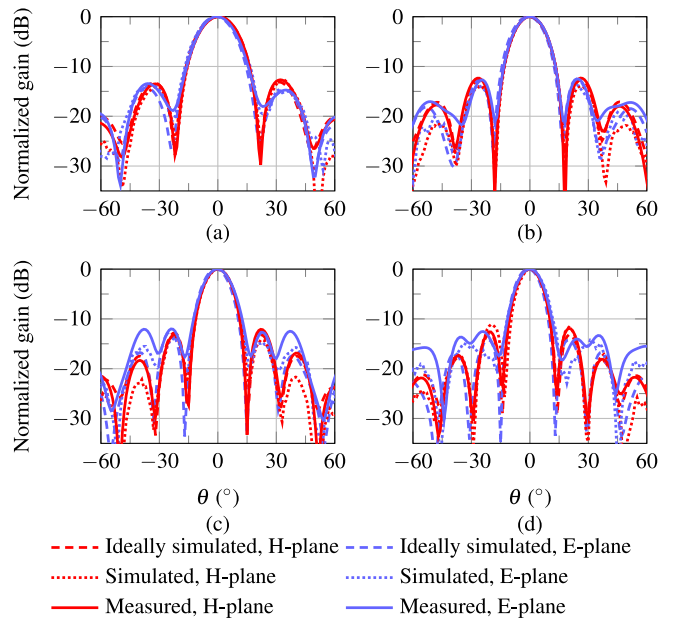
FIGURE 10. Comparison of the simulated and measured phase of the E-field in front of the aperture of the 8×8 array shown for each element at (a) 26 GHz, (b) 32 GHz, (c) 37 GHz, and (d) 40 GHz. The x- and y-axis represent the horizontal and vertical element number, and the color represents the phase of the E-field. Two instances of simulated results are represented: a raw simulation with the same phase in each antenna port and a simulation with calibrated phase corresponding to the measured phase on top of each antenna element.

FIGURE 11. Simulated and measured broadside patterns where in the second simulations the phases in the antenna element feed signals correspond to the measured phases in each antenna element feed at (a) 26 GHz, (b) 32 GHz, (c) 37 GHz, and (d) 40 GHz.

FIGURE 12. Simulated and measured gain of the 8×8 array. Two simulations are presented: one where all the antenna elements are fed in phase, and one where the phase of the fed signals is modified such that it represents more closely the measured antenna.
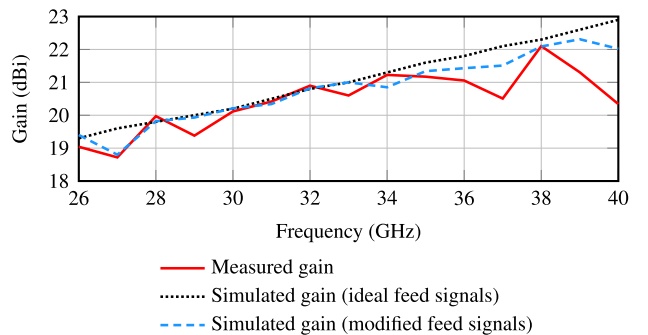
than in the rest of the elements. At 40 GHz in the designed feed network, an 80° phase shift in the stripline corresponds approximately to 0.9 mm. The result appears to be consistent with the type of the feed lines the elements are fed. The elements with the largest variation in phase when compared to the center element have a larger portion of stripline when the central elements are mostly microstrip lines with short stripline transitions. The result indicates that there could be a small inconsistency between the simulated and manufactured model resulting in increased electrical length in some of the feed lines. However, it appears the manufactured are very close to the designed dimensions when inspected under a microscope.

When the simulation is correlated with the data from the measurement, the simulation results agree well with the measurements, and similar phase patterns are observed. A comparison between the measured and simulated radiation patterns with correlated signals is shown in Fig. 11, exhibiting reasonable agreement. The radiation patterns of the initial simulation with ideal feed signals is shown for reference. The measured pattern differs mostly from the ideal simulation on the E-plane due to the flaw in the feed lines for the first and last rows.

The characterization of the losses in the feed network is a lot harder than the determination of the phase response.

Measuring the absolute magnitude of the transmission coefficient without a connector in each branch of the feeding network in place of the antenna array is basically impossible. Measuring the gain of the antenna array without the feeding network is also challenging if the loss in the feeding network is unknown. We use a compromise where the simulated loss of the feeding network is used to compensate for the network loss to estimate the gain of the array. The simulated gain of the antenna array and the estimation of the measured gain is shown in Fig. 12. The gain estimate is calculated by compensating the simulated feed network loss (8.5–14.7 dB) and using a SGH as a gain reference. The simulated results are performed with the bare antenna, where each element is fed directly from the coaxial feed line. The first simulation represents the ideal performance of the designed 8×8 array. In the ideal case, the gain increases linearly from

approximately 19.3 dBi to 22.9 dBi in the frequency range from 26 to 40 GHz. The second simulation represents the gain of the array when the signals feeding the elements are modified with the measured phases shown in Fig. 8 to better compare the measured and simulated results. In this simulation, we see some variation from the ideal gain especially at 27 GHz and at 40 GHz. The measured results are close to the simulated values and behave in a manner similar to the second simulation where the phase of the antenna elements is taken into account. At 37, 39, and 40 GHz, the measured gain is lower than the simulated values.

The results of the gain measurement can also be used to evaluate the performance of the interface between the antenna and the PCB. Overall, except for a couple of frequency points, the measured results with the simulated feed network loss is very close to the level of the simulated results, indicating that the interface is well aligned with the PCB and the antenna has good contact with the feeding pads on the PCB.

C. BEAM STEERING RESULTS

The performance of a beam-steerable antenna array can be represented, for example, with the scan loss and the level of the cross-polarization within the beam-steering range. First, the beam-steering performance of the antenna element is optimized with unit-cell simulations that emulate the performance of an infinite array. Then, a finite array of desired size is simulated, and the simulation results are compared with measured results of a manufactured array of the same size.

In unit-cell simulations, the scan loss follows very closely the ideal cosine curve on the E- and H-planes [19]. On the diagonal planes, the co-polarized scan loss is higher than on the elementary planes due to the increased cross-polarization. Although the antenna array operational band extends from 26 to 40 GHz, the comparison of the measured and simulated performance concentrates on the band between 32 and 37 GHz due to the limitation set by the phase shifters. Simulation results of the 8×8 array are additionally presented at the edge frequencies of the designed band at 26 and 40 GHz.

The 8×8 antenna array is simulated and measured with a varying progressive phase shift applied to the antenna elements. The radiation pattern of each element is simulated and the patterns are combined in post-processing. In the simulations, the beam is steered densely in the half sphere whereas the measurements are performed in a set number of points with a fixed progressive phase shift. The phase shifts for the measurements are calculated so that the resulting radiation patterns cover the steering range up to 68° away from the broadside direction at 37 GHz. The directions of the steered beams are presented in the standard spherical coordinate system where θ is the angular deviation from the z-axis or the broadside direction and ϕ is the angular deviation from the x-axis [23]. The selected 16 ϕ–planes are −165°, −135°, −105°, −90°, −75°, −45°, −15°, 0°, 15°, 45°, 75°,

TABLE 3. Steering angles θ which are the same for all the selected 16 ϕ-planes.

	32 GHz	34 GHz	35 GHz	37 GHz
θ_1	0°	0°	0°	0°
θ_2	12°	12°	11°	11°
θ_3	25°	23°	23°	21°
θ_4	38°	36°	34°	32°
θ_5	53°	48°	47°	43°
θ_6	61°	55°	53°	49°
θ_7	71°	63°	60°	55°
θ_8	90°	72°	68°	61°
θ_9		90°	78°	68°

90°, 105°, 135°, 165°, and 180° where planes $\phi = 0°$ and $\phi = 180°$ correspond to the H-plane while planes $\phi = −90°$ and $\phi = 90°$ correspond to the E-plane. A nonuniform spacing of the ϕ-planes is selected to increase the resolution of the results close to elementary planes where the largest change in the level of cross-polarization is observed without increasing the number of measurement points. The nine θ−angles are frequency dependent and these steering angles are shown in Table 3 at the measured frequency points. For 32 GHz, the largest progressive phase shift would result in the beam outside the visible angular range because of the dense element spacing. Therefore, the number of the measured beams is $1 + 16 \times 7 = 113$ at 32 GHz, i.e., the broadside beam and seven beams for each of the sixteen ϕ-planes. Similarly, the number of the measured beams is $1 + 16 \times 8 = 129$ at 34, 35, and 37 GHz, i.e., the broadside beam and eight beams for each of the sixteen ϕ-planes.

Although the resulting steering angles are relatively sparse, they give a good representation of the overall beam-steering performance that can be compared with the simulation results.

A similar method of calibration to the one used to match the simulated and measured phases in the previous section can be adapted to the measurements with the phase shifters. However, now the phase shifters are used to calibrate the feed network for more consistent phase across the array. The calibration is performed such that the array is initially measured without calibration and the phase of the E-field in front of each array element is compared with the ideally simulated values. The comparison is performed at 1 GHz interval and the average phase difference in the frequency points is used as the calibration value. This value is calculated for each array element and is then used as the initial state value for each phase shifter. When the antenna array is electrically steered these values are combined with the progressive phase shift. The phase of the E-field in front of the antenna elements after the calibration is shown in Fig. 13 at 32 and 37 GHz for the broadside radiation pattern. The variation in the measured phases in front of the elements is now less than 40°. The effect of the calibration can be seen in the Fig. 14 where measured radiation patterns with different steering angles are presented in E-, H-, and D-planes at 32 and 37 GHz. When comparing the broadside radiation pattern in Fig. 14 and Fig. 11, a difference between the broadside patterns especially at 37 GHz in the E-plane can
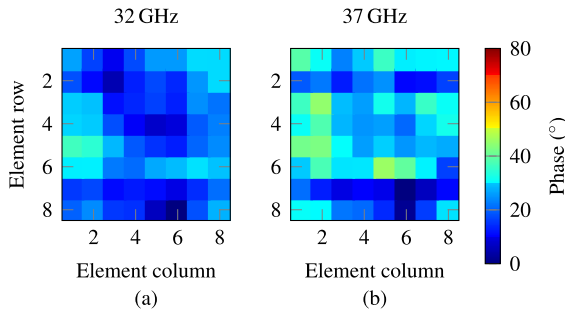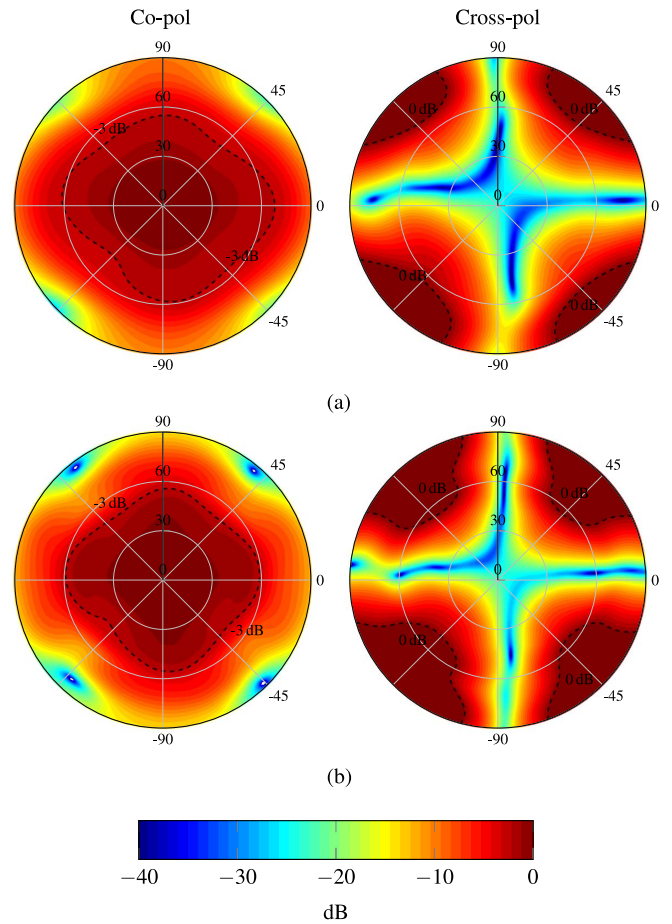
FIGURE 13. Measured phase of the E-field in front of the array with phase shifters shown for each element after calibration at (a) 32 GHz and (b) 37 GHz. The x- and y-axis represent the horizontal and vertical element number, and the color represents the phase of the E-field.
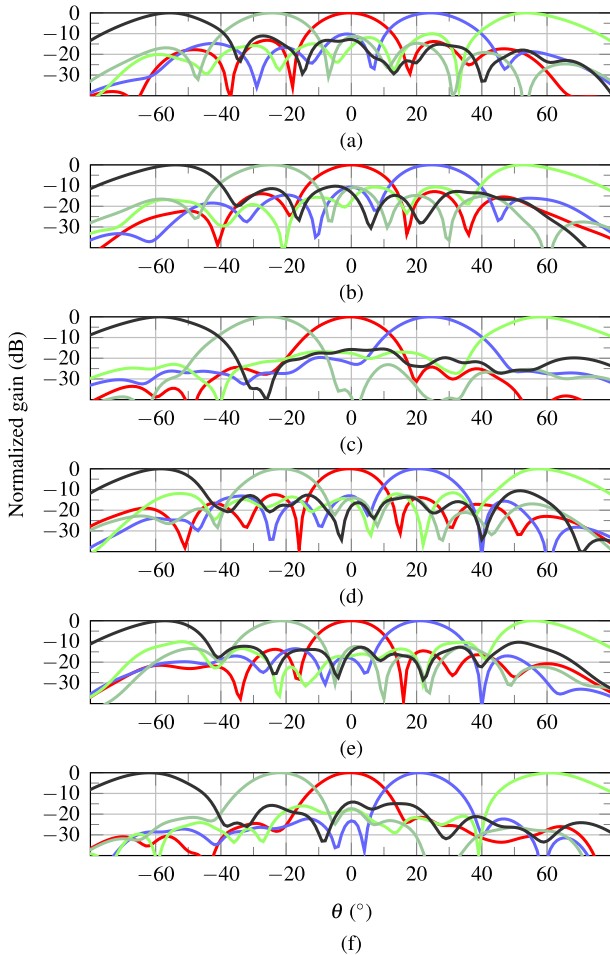
FIGURE 14. Measured normalized co-polarized radiation patterns of the antenna array with different steering angles after calibration. (a) 32 GHz in the E-plane, (b) 32 GHz in the H-plane, (c) 32 GHz in the D-plane, (d) 37 GHz in the E-plane, (e) 37 GHz in the H-plane, and (f) 37 GHz in the D-plane.

FIGURE 15. Simulated envelope of the co- polarized normalized gain and relative level of the cross-polarization at (a) 26 GHz and (b) 40 GHz.

be observed. In the uncalibrated case, the first and second side lobes are merged together. However, in the calibrated case the side lobes are properly separated and the pattern is closer to the ideal simulated pattern.

The scan performance of the co-polarized and cross-polarized data are presented as envelopes. The co-polarized envelopes are normalized to the broadside direction of the same plot at each frequency point. The cross-polarized data is represented as a relative value such that it is normalized to the co-polarized field in the same direction.

The simulated co-polarized and cross-polarized envelopes of the 8×8 antenna array at 26 and 40 GHz are shown in Fig. 15 and exhibit consistent behavior at both edges of the frequency band. Simulations corresponding to the measurement results at 32, 34, 35, and 37 GHz are shown in Fig. 16. The results follow well the unit-cell simulations, i.e., the cosine pattern. The dashed line in the co-polarized envelope represents the −3 dB scan loss. In all the cases the steering range with less than 3 dB of scan loss in E- and H-planes extends close to or beyond the 60° circle. In the diagonal planes, the scan loss is higher by 1–4 dB due to the increase in the cross-polarized field. When the level of the cross-polarization is close to the co-polarization in the diagonal planes with 60° steering, the resulting polarization is elliptical with a phase difference of 60° to 120° between the co- and cross-polarized fields.

The pattern in the envelope of the cross-polarization matches well with the theory and the unit-cell simulations. The cross-polarization is low in and close the E- and
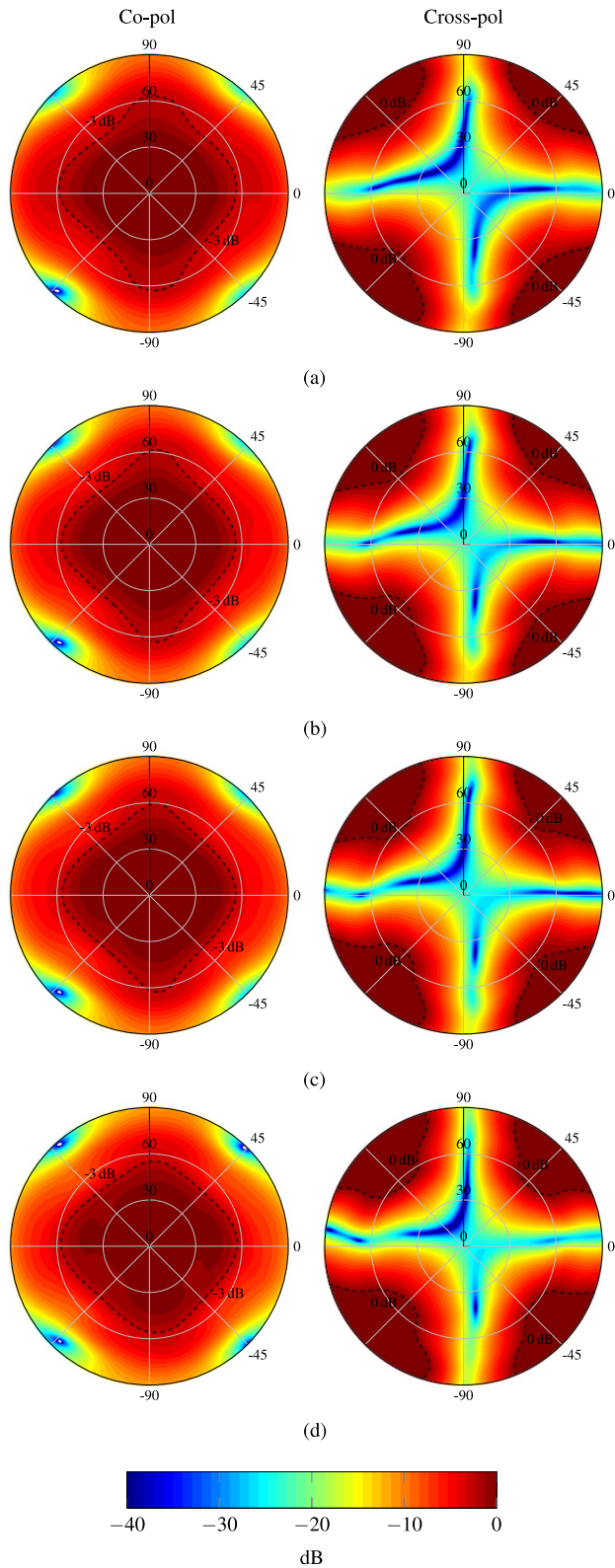
FIGURE 16. Simulated envelope of the co-polarized normalized gain and the relative level of the cross-polarization at (a) 32 GHz, (b) 34 GHz, (c) 35 GHz, and (d) 37 GHz.
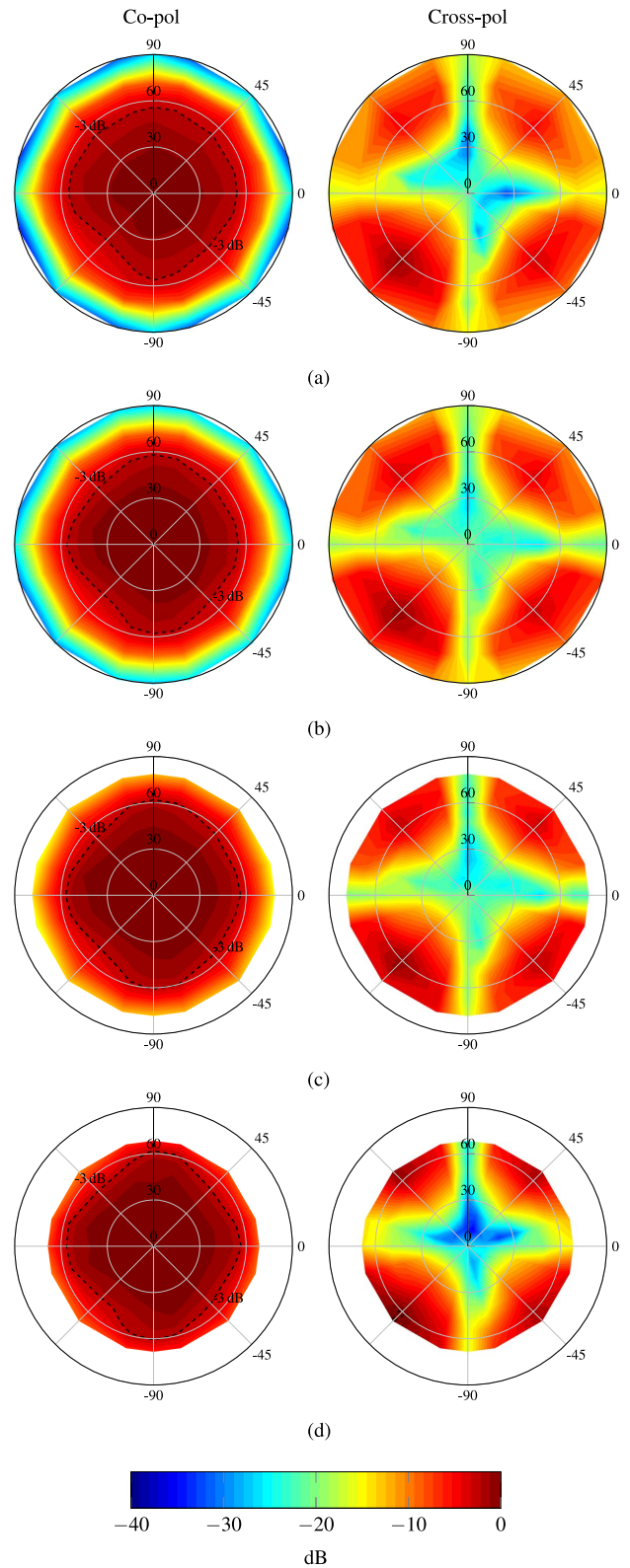
FIGURE 17. Measured envelope of the co-polarized normalized gain and the relative level of the cross-polarization at (a) 32 GHz, (b) 34 GHz, (c) 35 GHz, and (d) 37 GHz.

H-planes, and the level increases towards the diagonal planes when the beam is steered away from the broadside direction. In the lower left quadrant in the figures the cross-polarization

is observed to be higher than in the other quadrants. Similar behavior is also seen in the unit-cell simulations and it is caused by the asymmetric antenna elements due to the

90° bend in the antenna slot line to implement the vertical coaxial feed. The dashed line in the cross-polarization envelope represents the limit beyond which the cross-polarized field is stronger than the co-polarized. The figures only display values up to 0 dB, but the cross-polarization increases even higher at large steering angles close to the nulls in the co-polarized envelope.

The measured envelopes of the co- and cross-polarized fields are shown in Fig. 17. The antenna array behaves similarly in the measurements as in the simulations. The shape of the −3-dB contour line in the co-polarized envelope is similar to the simulations and can be seen to extend near the 60° circle in the E- and H-planes. The measured cross-polarized envelope pattern also displays a pattern similar to the simulations in the steering range. However, the details in the cross-polarized envelope cannot be seen as clearly as in the simulated results. The behavior in which the bottom-left quadrant displays higher cross-polarization is also visible in the measurements. This demonstrates that the simulated and measured performance agree well within approximately 60° from the broadside direction. The planar measurement setup limits the accurate angular range up to about 60°; beyond that the results are not reliable.

Although, the measurements are limited to the operation range of the phase shifters, the simulations of the same 8×8-array have been simulated from 26 GHz to 40 GHz, and they are in good agreement with the unit-cell simulations. The simulations between 26 and 32 GHz and between 37 and 40 GHz exhibit similar behavior, as already presented in Fig. 15. The co-polarized scan loss is close to 3 dB at steering angle 60° in the E- and H-planes whereas the level of the cross-polarization is high on the edges of the steering range away from the E- and H-planes.

IV. CONCLUSION

A surface-mounted fully metallic dual-polarized antenna array based on the Vivaldi element is proposed and manufactured. The feeding network for demonstrating the operation of the antenna array is designed and manufactured with a layout where one polarization of the 8×8 antenna array can be excited while the elements at the other polarization are terminated. Two variations of the layout are manufactured. In one layout the phase shifters are placed in line with feed lines to each antenna element to demonstrate the beam steering capability of the antenna array. In the other layout the phase shifters are replaced with a transmission line so that the antenna and the feed network can be more easily tested without the added complexity of the phase shifters.

Simulations demonstrate that the interface between the antenna and the PCB works well and is not prone to errors in the alignment of the feeding pad on the PCB and the coaxial center pin in the antenna. The interface is shown to easily handle a transversal displacement of 200 μm without any impact on the performance. The shift along the z-axis is more sensitive, and a gap of 15 μm or more between the

coaxial center pins and the feeding pads on the PCB starts to have a noticeable impact.

The antenna array is first measured with the feeding network without the phase shifters. The results indicate that a phase variation up to ±40° occurs between the elements. After correlating the phase shift in the simulations, the measured and simulated radiation patterns agree well. Similarly, the measured gain agrees well with the simulated result between 26 and 38 GHz. At most, at 39 and 40 GHz, the measured values are approximately 1 and 1.5 dB lower than the simulated values.

The scan performance of the antenna array is demonstrated. The demonstration is limited to the frequency range between 32 and 37 GHz due to the phase shifters. The measured results agree well with the simulations. In all the measured and simulated cases, the scan loss in the co-polarized patterns is approximately 3 dB when steered 60° in the E- and H-planes. Outside the close proximity of the elementary planes the increased cross-polarization increases the scan loss.

REFERENCES

[1] J. D. S. Langley, P. S. Hall, and P. Newham, "Balanced antipodal Vivaldi antenna for wide bandwidth phased arrays," *IEE Proc. Microw. Antennas Propag.*, vol. 143, no. 2, pp. 97–102, Apr. 1996.

[2] D. Schaubert, S. Kasturi, A. Boryssenko, and W. Elsallal, "Vivaldi antenna arrays for wide bandwidth and electronic scanning," in *Proc. 2nd Eur. Conf. Antennas Propag.*, Nov. 2007, pp. 1–6.

[3] J. Shin and D. H. Schaubert, "A parameter study of stripline-fed Vivaldi notch-antenna arrays," *IEEE Trans. Antennas Propag.*, vol. 47, no. 5, pp. 879–886, May 1999.

[4] R. W. Kindt and J. T. Logan, "Benchmarking ultrawideband phased antenna arrays: Striving for clearer and more informative reporting practices," *IEEE Antennas Propag. Mag.*, vol. 60, no. 3, pp. 34–47, Jun. 2018.

[5] R. W. Kindt and W. R. Pickles, "Ultrawideband all-metal flared-notch array radiator," *IEEE Trans. Antennas Propag.*, vol. 58, no. 11, pp. 3568–3575, Nov. 2010.

[6] J. B. Yan, S. Gogineni, B. Camps-Raga, and J. Brozena, "A dual-polarized 2–18-GHz Vivaldi array for airborne radar measurements of snow," *IEEE Trans. Antennas Propag.*, vol. 64, no. 2, pp. 781–785, Feb. 2016.

[7] H. Holter, "Dual-polarized broadband array antenna with BOR-elements, mechanical design and measurements," *IEEE Trans. Antennas Propag.*, vol. 55, no. 2, pp. 305–312, Feb. 2007.

[8] H. Holter, T.-H. Chio, and D. H. Schaubert, "Experimental results of 144-element dual-polarized endfire tapered-slot phased arrays," *IEEE Trans. Antennas Propag.*, vol. 48, no. 11, pp. 1707–1718, Nov. 2000.

[9] Z. Hao, W. Hong, J. X. Chen, X. P. Chen, and K. Wu, "A novel feeding technique for antipodal linearly tapered slot antenna array," in *IEEE Int. Microw. Symp. Dig. (MTT-S)*, 2005, pp. 1641–1643.

[10] J. T. Logan, R. W. Kindt, and M. N. Vouvakis, "A 1.2–12 GHz sliced notch antenna array," *IEEE Trans. Antennas Propag.*, vol. 66, no. 4, pp. 1818–1826, Apr. 2018.

[11] S. Zhu, H. Liu, Z. Chen, and P. Wen, "A compact gain-enhanced Vivaldi antenna array with suppressed mutual coupling for 5G mmWave application," *IEEE Antennas Wireless Propag. Lett.*, vol. 17, no. 5, pp. 776–779, May 2018.

[12] J. Kurvinen, H. Kähkönen, A. Lehtovuori, J. Ala-Laurinaho, and V. Viikari, "Co-designed mm-wave and LTE handset antennas," *IEEE Trans. Antennas Propag.*, vol. 67, no. 3, pp. 1545–1553, Mar. 2019.

[13] X. Luo *et al.*, "A scalable Ka-band 1024-element transmit dual-circularly-polarized planar phased array for SATCOM application," *IEEE Access*, vol. 8, pp. 156084–156095, 2020.

[14] J. C. S. Chieh *et al.*, "Development of flat panel active phased array antennas using 5G silicon RFICs at Ku- and Ka-bands," *IEEE Access*, vol. 8, pp. 192669–192681, 2020.

[15] J. Du *et al.*, "Dual-polarized patch array antenna package for 5G communication systems," in *Proc. 11th Eur. Conf. Antennas Propag. (EUCAP)*, 2017, pp. 3493–3496.

[16] T. Lambard, O. Lafond, M. Himdi, H. Jeuland, S. Bolioli, and L. L. Coq, "Ka-band phased array antenna for high-data-rate SATCOM," *IEEE Antennas Wireless Propag. Lett.*, vol. 11, pp. 256–259, 2012.

[17] R. Valkonen, "Compact 28-GHz phased array antenna for 5G access," in *Proc. IEEE/MTT-S Int. Microw. Symp. (IMS)*, 2018, pp. 1334–1337.

[18] A. Chen, Y. Zhang, Z. Chen, and C. Yang, "Development of a Ka-band wideband circularly polarized 64-element microstrip antenna array with double application of the sequential rotation feeding technique," *IEEE Antennas Wireless Propag. Lett.*, vol. 10, pp. 1270–1273, 2011.

[19] H. Kähkönen, J. Ala-Laurinaho, and V. Viikari, "Dual-polarized Ka-band Vivaldi antenna array," *IEEE Trans. Antennas Propag.*, vol. 68, no. 4, pp. 2675–2683, Apr. 2020.

[20] "Eccosorb MF lossy, magnetically loaded, machinable stock," Eccosorb Data Sheet, Laird, Chesterfield, MO, USA, Nov. 2018.

[21] "Qorvo TGP2102 35 GHz 5-bit digital phase shifter," Data Sheet TGP2102, Qorvo, Greensboro, NC, USA, May 2019.

[22] "High speed, low loss multi-layer materials Megtron7," Megtron7 Data Sheet, Panasonic, Kadoma, Japan, Jul. 2019.

[23] *IEEE Standard Test Procedures for Antennas*, ANSI/IEEE Standard 149-1979, 1979, pp. 1–129.

JUHA ALA-LAURINAHO received the Diploma Engineering (M.Sc.) degree in mathematics and the D.Sc. (Tech.) degree in electrical engineering from the TKK Helsinki University of Technology, Finland, in 1995 and 2001, respectively.

He has been with the TKK, currently, Aalto University, serving in the Radio Laboratory from 1995 to 2007, in the Department of Radio Science and Engineering from 2008 to 2016, and currently serves as a Staff Scientist in the Department of Electronics and Nanoengineering. He has been a Researcher and a Project Manager on many millimeter-wave technology-related projects. His current research interests are the antennas and antenna measurement techniques for millimeter and submillimeter waves, and the millimeter-wave imaging.

VILLE VIIKARI (Senior Member, IEEE) was born in Espoo, Finland, in 1979. He received the Master of Science (Tech.) and the Doctor of Science (Tech.) (with Distinction) degrees in electrical engineering from the Helsinki University of Technology (TKK), Espoo, in 2004 and 2007, respectively.

He is currently an Associate Professor and the Deputy Head of Department with the School of Electrical Engineering, Aalto University. From 2001 to 2007, he was with the Radio Laboratory, TKK, where he studied antenna measurement techniques at submillimeter wavelengths and antenna pattern correction techniques. From 2007 to 2012, he was a Research Scientist and a Senior Scientist with VTT Technical Research Centre, where his research included wireless sensors, RFID, radar applications, MEMS, and microwave sensors. His current research interests include antennas for mobile networks, RF-powered devices, and antenna measurement techniques.

Dr. Viikari was a recipient of the Young Researcher Award of the Year 2014, presented by the Finnish Foundation for Technology Promotion, the IEEE Sensors Council 2010 Early Career Gold Award, the 2008 Young Scientist Award of the URSI XXXI Finnish Convention on Radio Science, Espoo, and the Best Student Paper Award of the Annual Symposium of the Antenna Measurement Techniques Association, Newport, RI, USA (October 30–November 4, 2005). He has served as the Chair of the Technical Program Committee of the ESA Workshop on Millimetre-Wave Technology and Applications and the Global Symposium on Millimeter Waves twice, in 2011 and 2016 in Espoo.

HENRI KÄHKÖNEN was born in Lohja, Finland, in 1989. He received the B.Sc. (Tech.) and M.Sc. (Tech.) degrees in electrical engineering from Aalto University, Espoo, Finland, in 2015 and 2017, respectively. He is currently pursuing the D.Sc. (Tech.) degree with Saab Ab and with the Department of Electronics and Nanoengineering, School of Electrical Engineering, Aalto University, where he has been a Research Assistant since 2016. His current research interests include wideband, beam steerable antenna arrays, especially at millimeter-wave spectrum.